Microwave susceptibility analysis of ultrafast moment dynamics in a multicore magnetic nanoparticle system

Menghao Li [1] Suko Bagus Trisnanto [1,*] Yasushi Endo [2,3] Satoshi Ota [4] Teruyoshi Sasayama [5]
Takashi Yoshida [5] and Yasushi Takemura [1]

[1]*Department of Electrical and Computer Engineering, Yokohama National University, Yokohama 240-8501, Japan*
[2]*Department of Electrical Engineering, Tohoku University, Sendai 980-8579, Japan*
[3]*Center for Science and Innovation in Spintronics, Tohoku University, Sendai 980-8577, Japan*
[4]*Department of Electrical and Electronic Engineering, Shizuoka University, Hamamatsu 432-8561, Japan*
[5]*Department of Electrical and Electronic Engineering, Kyushu University, Fukuoka 819-0395, Japan*

Room-temperature magnetization dynamics of multicore magnetic nanoparticles often account for intrinsic dipolar magnetism to behave as a single macrospin at low-frequency regime. Either magnetic particle imaging or hyperthermia benefits from the resulting superparamagnetism in terms of nonlinear magnetization response and relaxation losses at frequencies where the rotation of magnetic moments dominates over Brownian motion for a given sinusoidal field. For this situation, spontaneous thermal relaxation (in the absence of external fields) of each composing particle moment within the cluster is critical to define effective Néel time constant and may intersect with ferromagnetic resonance (FMR) at GHz range. Here, we performed broadband AC susceptometry on both immobilized single-core and multicore iron-oxide nanoparticles up to 26.5 GHz under DC bias fields. For each solid sample, we confirmed FMR frequency, where large single-core nanoparticle systems demonstrated typical resonance blueshift as DC field increased. Interestingly, high DC field induced the secondary satellite peak in the imaginary part of AC susceptibility spectra for the case of multicore nanoparticle systems. We further highlighted that a synchronous precession of the polarized macrospins under nonuniform effective fields was responsible for splitting FMR peaks at nearby microwave frequencies. Upon curve fitting of the field-dependent FMR frequency spectra, the Landau-Lifshitz-Gilbert-Kittel model later elaborates on the complex moment dynamics of multicore nanoparticle systems in correlation with distribution functions.

I. INTRODUCTION

Biocompatible iron-oxide particles with diameters of a few nanometers can form a single magnetic domain that behaves as a giant moment, or macrospin, due to the unidirectional arrangement of atomic spins. If these particles possess uniaxial anisotropy, their magnetic moments may flip randomly across the easy axis at room temperature when thermal agitation overcomes the anisotropic energy barrier [1,2]. During particle synthesis, controlling either nucleation or growth thermally and stoichiometrically can produce superparamagnetic nanoparticles and their superstructures (e.g., nanoflowers) [3]. For biomedical applications such as magnetic hyperthermia [4,5], surface modification of particles is necessary to facilitate steric and electrostatic stabilization in a liquid medium [6]; however, this may potentially lead to secondary particle clustering [7]. Despite this, multicore magnetic nanoparticles exhibit excellent nonlinear magnetization properties suitable for magnetic particle imaging [8,9].

Multicore magnetic nanoparticles, which are aggregates of small superparamagnetic cores, exhibit room-temperature superparamagnetism [10]. To discuss this unique magnetization response in thermal equilibrium, the Langevin function emphasizes the ratio of the Zeeman magnetopotential to thermal energy, where the particle moments and their distribution significantly affect the linearity of the curve for given external magnetic fields. Moreover, the time necessary for multicore nanoparticles to minimize magnetopotential generally correlates with magnetization reversal due to the rotations of both the hydrodynamic volumes and the composing magnetic moments. The Brownian alignment of the easy axis positively contributes to low-frequency magnetization dynamics, whereas rotational friction may immobilize clusters undergoing high-frequency relaxation [11]. Although the coexistence of Brownian and Néel relaxations complicates the analysis of magnetization dynamics [12], it can be simplified by considering only the behavior of magnetic moments as the dominant mechanism in solidified aggregates [13].

The Néel relaxation time (τ_N) of core particles with small anisotropic energy is principally faster than Brownian rotation of the aggregates. In the Néel-Arrhenius model, $\tau_N = \tau_0 \exp(\sigma)$, the characteristic relaxation time τ_0 is often assumed to be between 10^{-9} and 10^{-10} s, with σ representing the ratio of anisotropy energy to thermal energy. However,

*Contact author: suko-trisnanto-zt@ynu.ac.jp

thermal relaxation also depends on the decay time of the Larmor precession with a damping factor α, where an external magnetic field drives the moments to perform gyroscopic rotation around the effective field ($\mathbf{H}_{\text{eff}}$) with an angular frequency of $\omega_0 = \gamma H_{\text{eff}}$ for $H_{\text{eff}} = |\mathbf{H}_{\text{eff}}|$. These fast magnetization dynamics ($\mathbf{M}$) can be further described by the Landau-Lifshitz-Gilbert (LLG) equation

$$\frac{d\mathbf{M}}{dt} = -\gamma \mathbf{M} \times \mathbf{H}_{\text{eff}} + \frac{\alpha}{M_s} \mathbf{M} \times \frac{d\mathbf{M}}{dt}, \qquad (1)$$

where γ is gyromagnetic ratio and M_s is the saturation magnetization [14]. When sinusoidal fields with frequency $\omega_0/2\pi$ are applied, magnetic moments resonate as they absorb microwave power, a phenomenon known as ferromagnetic resonance (FMR) [15]. Characterizing both the Néel relaxation and the FMR spectra of multicore magnetic nanoparticles is crucial for biomedical applications.

The spectral magnetization response of magnetic nanoparticles is often analyzed using AC susceptometry, which measures the frequency dependence of the complex magnetic susceptibility $\chi(\omega) = \chi'(\omega) - i\chi''(\omega)$. The real part, χ', indicates the magnetization component in the direction of the applied AC magnetic field, whereas the imaginary part, χ'', represents the phase difference between the magnetization and the field. Due to the different characteristics of the longitudinal ($\chi_\parallel$) and transverse ($\chi_\perp$) magnetic susceptibility spectra relative to the easy axis of magnetization, relaxation and FMR can be observed as a collective magnetization response in terms of $\chi(\omega) = (\chi_\parallel + 2\chi_\perp)/3$ [16]. For a small σ, the magnetic moment is significantly affected by thermal disturbances, so the relaxation and resonance phenomena may coexist at nearby frequencies [17]. Meanwhile, a large σ results in moment rigidity (i.e., thermally blocked moment dynamics) with a longer relaxation time. Similarly, multicore nanoparticles can be treated as a single entity with a large effective core whose size is determined by the internal activation energy [18]. Because the dipole interactions and the effective anisotropy field of the core particles are substantial at nanosecond timescales [19,20], FMR should be further distinguished from Néel relaxation when employing a DC bias field to adjust the energy barrier.

The microwave-frequency magnetization response is an important property of multicore magnetic nanoparticles; however, experimental studies are lacking. In this study, we performed broadband AC susceptometry to demonstrate the different moment behaviors of an immobilized multicore nanoparticle system compared to a typical single-core system. We began with theoretical reviews of the Néel relaxation and FMR of magnetic nanoparticles as the basis for our methodology for measuring GHz AC susceptibility of nanoparticle samples. We then correlated the static field dependence of the complex susceptibility spectra with the moment relaxation and FMR characteristics while considering the distribution functions. Here, we applied the Debye and LLG-Kittel models to numerically fit the susceptibility spectra attributed to relaxation and resonance phenomena, respectively. This paper highlights how the moment dynamics of multicore nanoparticles changes under a polarizing DC field, revealing unique dual-mode FMR frequency spectra.

II. MOMENT RELAXATION AND RESONANCE

A. Thermal relaxation

Under an external AC field ($\mathbf{H}_{\text{AC}}$) relative to the anisotropy field ($\mathbf{H}_a$), the magnetic moment ($\mathbf{m}$) of an immobilized nanoparticle tends to oscillate in the direction of the effective field [Fig. 1(a)]. A monodomain nanoparticle typically follows the Debye equation to describe its relaxation behavior, as shown in Eq. (2) [21]:

$$\chi_\parallel(\omega) = \frac{\chi_{\parallel,0}}{1 + i\omega\tau}. \qquad (2)$$

Both the equilibrium susceptibility ($\chi_{\parallel,0}$) and the effective relaxation time (τ) depend on the field amplitude. For an elliptical ferromagnetic nanoparticle with uniaxial anisotropy, the Stoner-Wohlfarth model emphasizes the hysteresis in the magnetization response corresponding to minimized internal energy as a function of the angle between the magnetization and the applied field relative to the easy axis [22]. In the case of spherical nanoparticles with small anisotropy, thermal-energy-augmented random torques activate spontaneous moment relaxation, where the time constant $\tau \approx \tau_N$ can be estimated from Brown's eigenfunctions, as shown in Eq. (3) [23,24]:

$$\tau_N = \begin{cases} \frac{\tau_0 \sqrt{\pi}}{2\sqrt{\sigma}} \exp \sigma, & \sigma \geqslant 1 \\ \tau_0 \sigma \left(1 - \frac{2}{5}\sigma + \frac{48}{875}\sigma^2\right)^{-1}, & \sigma \ll 1. \end{cases} \qquad (3)$$

In Eq. (3), $\sigma = K_u V_m/(k_B T)$ considers the particle volume (V_m) and ambient temperature (T) as critical parameters for observing superparamagnetism, whereas K_u and k_B are the anisotropy and Boltzmann constants, respectively.

In the absence of external fields, the magnetic moments of noninteracting superparamagnetic nanoparticles freely rotate at the Néel relaxation frequency $f_N = (2\pi\tau_N)^{-1}$, randomizing the magnetization vectors. As illustrated in panel (i) of Fig. 1(a), the normalized AC susceptibility spectra $[\chi_\parallel(\omega)/\chi_{\parallel,0}]$ of the Debye model describe that very low AC fields with a frequency $f \ll f_N$ allow the moments to oscillate their vectors across the field direction without a phase difference. When f approaches f_N, moment relaxation has a time lag relative to the magnetic field and a decreased oscillation amplitude, as shown in panel (ii) of Fig. 1(a). For $f = f_N$, $\chi_\parallel''$ is maximized and equals $\chi_\parallel'$, resulting in a phase difference $\varphi = \tan^{-1}(f/f_N) = \pi/4$ [panel (iii) of Fig. 1(a)]. This creates the largest relaxation loss, which is typically used for magnetic hyperthermia. Furthermore, when $f > f_N$, the moments are unable to fully rotate during the observation time, thereby reducing the apparent magnetic susceptibility [panel (iv) of Fig. 1(a)]. In the GHz range, the Larmor precession eventually becomes significant to define moment dynamics [25,26].

B. Magnetic resonance

Three-dimensional gyroscopic motion of magnetic moments occurs at the Larmor frequency. When an additional DC field ($\mathbf{H}_{\text{DC}}$) is applied, the parallel alignment of moments leads to FMR, depending on the field intensity. This resonance mode causes magnetic moments to precess around $\mathbf{H}_{\text{eff}}$ direction, which is the resultant vector of anisotropy and the
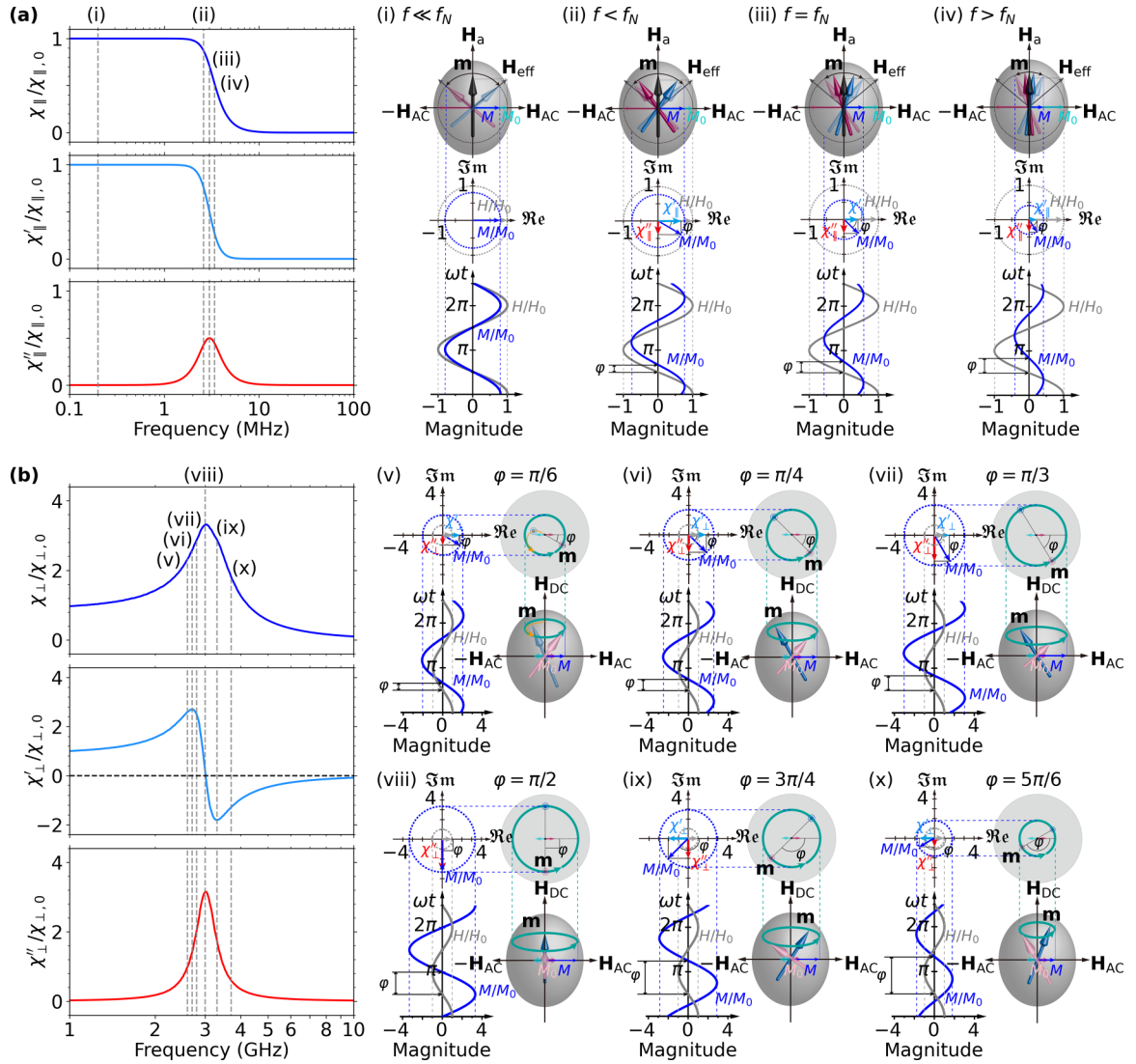
FIG. 1. Moment dynamics of an elliptical ferromagnetic nanoparticle involving (a) Debye relaxation and (b) LLG-Kittel resonance behaviors. Complex (parallel) susceptibility spectra $\chi_\parallel$ of the Debye relaxation model has positive values for both the real ($\chi_\parallel'$) and imaginary ($\chi_\parallel''$) parts normalized to the equilibrium susceptibility $\chi_{\parallel,0}$. Panels (i)–(iv) illustrate moment oscillation at different frequencies relative to the Néel relaxation frequency $f_N = 3$ MHz with phase delay $\varphi = 0$, $\pi/6$, $\pi/4$, and $\pi/3$, respectively. Under sinusoidal excitation $\mathbf{H}_{AC}$ and anisotropy field $\mathbf{H}_a$ that create an effective field $\mathbf{H}_{eff}$, particle moment $\mathbf{m}$ reorients its vector to minimize magnetopotential energy. In terms of the scalar quantity, apparent magnetization M relative to its quasistatic value M_0 at arbitrary temperature decreases with increasing frequency of the applied field H with amplitude H_0. FMR behavior results in the complex (perpendicular) susceptibility spectra $\chi_\perp$ with negative real parts ($\chi_\perp'$) and positive imaginary parts ($\chi_\perp''$) normalized to $\chi_{\perp,0} = \alpha\gamma M_s$. For $\alpha = 0.1$ and $\omega_0/(2\pi) = 3$ GHz, panels (v)–(x) depict the moment precession, where φ of M/M_0 relative to H/H_0 equals $\pi/6$, $\pi/4$, $\pi/3$, $\pi/2$, $3\pi/4$, and $5\pi/6$, respectively.

DC bias fields. As shown in Fig. 1(b), the resonance characteristics of the frequency-dependent perpendicular susceptibility can be expressed using the LLG-Kittel model in Eq. (4) [27]:

$$\chi_\perp(\omega) = \frac{\gamma M_s(\omega_0 + i\alpha\omega)}{\omega_0^2 - \omega^2(1 + \alpha^2) + 2i\alpha\omega_0\omega}. \quad (4)$$

At $f < f_r$ [panels (v)–(vii) of Fig. 1(b)], $\chi_\perp'$ initially has a nonzero value, allowing a slight moment rotation under $\mathbf{H}_{AC}$ perpendicular to $\mathbf{H}_{eff}$. As f increases, the magnetic moments precess, and the resulting oscillatory magnetization response lags behind $\mathbf{H}_{AC}$ with a phase difference φ. A large precession angle maximizes $\chi_\perp'$ at $\varphi = \pi/4$ [panel (vi) in Fig. 1(b)]. Despite the large values of φ and $\chi_\perp = (\chi_\perp'^2 + \chi_\perp''^2)^{1/2}$, $\chi_\perp'$

decreases to zero at the FMR frequency $f_r = \omega_0/(2\pi\sqrt{1-\alpha^2})$.

Unlike Debye relaxation, FMR behavior results in $\varphi = \pi/2$ to maximize $\chi_\perp''$, as the absorbed microwave power energizes the moment precession [panel (viii) of Fig. 1(b)]. Therefore, the amplified magnetization response peaks at $f = f_r$. During the relaxation process at any frequency, $\chi_\parallel'$ is always a non-negative value with $0 \leqslant \varphi \leqslant \pi/2$. In contrast, moment precession allows φ to exceed $\pi/2$ for $f > f_r$, where the in-phase component of the magnetization has a direction opposite to that of $\mathbf{H}_{AC}$ [panel (ix) of Fig. 1(b)]. This situation leads to negative $\chi_\perp'$. For $f \gg f_r$, the moment dynamics later converge in the direction of $\mathbf{H}_{eff}$ with $\chi_\perp = 0$ owing to the

damping term in Eq. (1) [28]. From Fig. 1, we expect overlapping relaxation and FMR frequency spectra for the magnetic nanoparticle system at $\mathbf{H}_{DC} = 0$. The effects of single-core and multicore structures should be observable when random fields due to thermal agitation are trivial in comparison to the magnetopotential at large $\mathbf{H}_{DC}$.

III. MATERIALS AND METHODS

A. Sample preparation

To test our hypothesis, we prepared four polydisperse iron-oxide nanoparticle samples with an equivalent iron concentration of $46\,\mathrm{mg_{Fe}\,mL^{-1}}$ to investigate their magnetic moment dynamics in the microwave range, namely, samples S0, S1, S2, and S3. As a reference for analytical comparison, we used sample S0 (M300, Sigma Hi-Chemical, Japan) consisting of magnetite nanoparticles coated with sodium α-olefin sulfonate, and treated it as a single-core nanoparticle system due to its large particle size, which is comparable to its hydrodynamic volume. Sample S1 (Ferucarbotran, Meito-Sangyo Co. Ltd., Japan) contains carboxydextran-coated multicore maghemite nanoparticles with a broadened moment distribution [29]. Ferucarbotran has been used as an active pharmaceutical ingredient in Resovist® for magnetic resonance imaging contrast agents. To estimate the cluster size, we initially measured the room-temperature AC magnetic susceptibility of the liquid samples S0 and S1 below 10 MHz (Appendix A). Then, we obtained hydrodynamic diameters (D_s) of 30.5 and 58.5 nm from the Brownian relaxation time $\tau_B = \pi \eta D_s^3 / (2 k_B T)$, maximizing $\chi''(\omega)$ at frequency $f_B = (2\pi \tau_B)^{-1}$. Here, the dynamic viscosities (η) of samples S0 and S1 are 1.35 and 1.28 mPas at $T = 295$ K, respectively.

Thermal relaxation can be blocked by a large anisotropy barrier, depending on the particle size. Similarly, intrinsic dipolar interactions lead to a longer τ_N [30]. To control this, sample S1 was magnetically fractionated to obtain samples S2 and S3, which have different moment distributions but similar primary core sizes and hydrodynamic volumes. For GHz-band AC susceptometry, all samples were solidified with epoxy resin to ensure that the respective nanoparticles had a random orientation. To prepare these samples, we uniformly mixed epoxy resin (including hardener) with a nanoparticle suspension at a volume ratio of 1:1. The mixture was allowed to solidify at room temperature for more than 8 h before sample cutting. The static magnetization characteristics of the solid samples were measured using a vibrating-sample magnetometer (VSM Model 3, Toei Industry Co. Ltd., Japan) and fitted using a double-weighted Langevin function to obtain the magnetic moment distribution of the primary and secondary cores (Appendix B). The VSM employed a large electromagnet system with a diameter of 0.6 m to produce a uniform spatial distribution of static fields covering the sample volume.

As shown in Fig. 2, sample S0 exhibits a broadening moment distribution with a single mode at $2.24 \times 10^{-19}\,\mathrm{A\,m^2}$. The equivalent (primary) core size can be estimated as $D_p = [6\bar{m}_p / (\pi M_s)]^{1/3}$, where $\bar{m}_p / M_s$ is the mean particle moment normalized by the saturation magnetization. In contrast, sample S1 appears to have a bimodal moment distribution
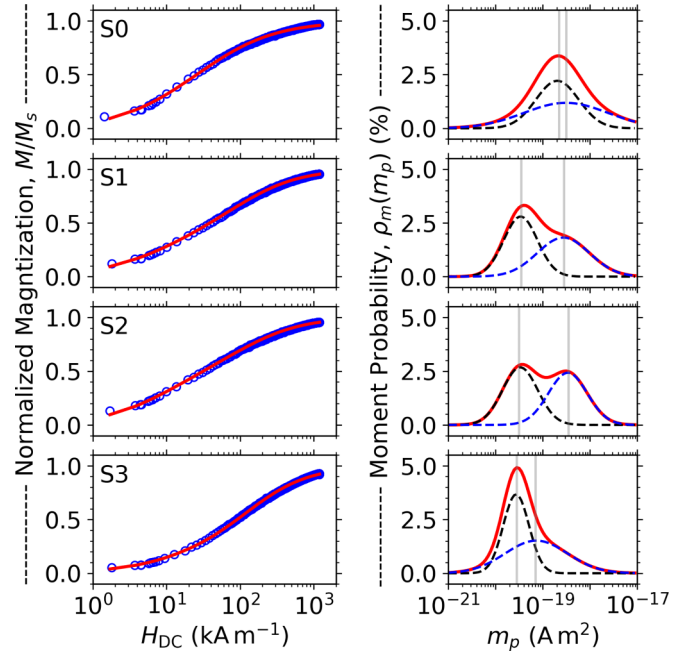

FIG. 2. Numerical computation of static magnetization curve (M/M_s) and magnetic moment distribution (ρ_m) of nanoparticle samples. Open circles indicate the VSM reading normalized to each saturation magnetization (M_s). ρ_m (m_p) is obtained by curve fitting of M/M_s using the Langevin function (red lines). Black and blue dashed lines indicate the primary and secondary moment distributions, respectively, with a total probability ratio of 1:1.

attributed to the core and cluster moments. Magnetic fractionation allows sample S3 to have smaller secondary core size than sample S2, which was associated with the different values of $\bar{m}_p$ in each secondary moment distribution. Table I summarizes the physical properties of all samples, where $\bar{m}_p = \sum_{i=1}^{N} \rho_{m,i} m_{p,i}$ is obtained from the primary moment distribution (Fig. 2). For a total number N of discretized particle moments, $\rho_{m,i}$ expresses the probability of the ith moment such that $\sum_{i=1}^{N} \rho_{m,i} = 0.5$ in each subdistribution. In Table I, M_s is treated as the volume magnetization by multiplying the VSM reading per unit mass (in $\mathrm{A\,m^2\,kg^{-1}}$) with a mass density of 5150 and 4900 $\mathrm{kg\,m^{-3}}$ for the magnetite and maghemite samples, respectively.

B. Nanoparticle model

Multicore nanostructures can be modeled as an assembly of superparamagnetic nanoparticles densely packed into

TABLE I. Physical properties of nanoparticle samples extracted from magnetization responses.

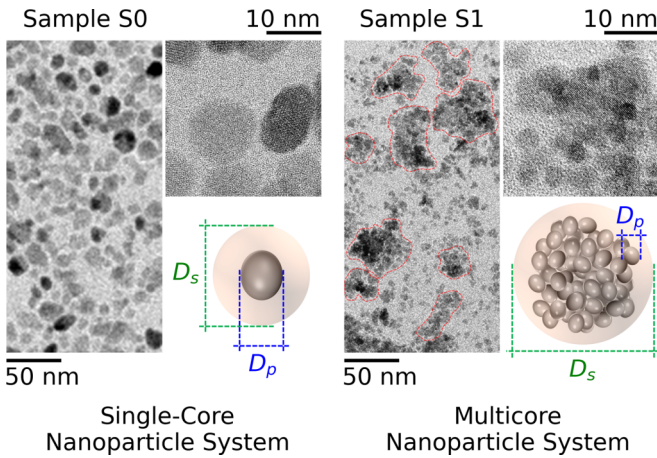| Sample	Main content	M_s (kA m^{-1})	$\bar{m}_p$ (A m^2)	D_p (nm)	D_s (nm)	$\frac{D_p}{D_s}$
S0	Fe$_3$O$_4$	410.1	3.49×10^{-19}	11.76	30.5	0.39
S1	γFe$_2$O$_3$	324.3	4.79×10^{-20}	6.56	58.5	0.11
S2	γFe$_2$O$_3$	314.9	4.83×10^{-20}	6.64	60.5	0.11
S3	γFe$_2$O$_3$	353.0	3.35×10^{-20}	5.66	61.7	0.09

FIG. 3. TEM images and nanoparticle models of samples S0 and S1. D_p is the primary core diameter defined by the static magnetization response, whereas D_s is the hydrodynamic diameter estimated from the Brownian relaxation time of the particles. Based on the ratio of D_p/D_s, samples S0 and S1 were modeled as single-core and multicore nanoparticle systems, respectively. Red lines indicate the clustered particles in sample S1, which are recognized as secondary cores.

a cluster with rigid Brownian rotation in a liquid medium [31]. Because of particle clustering, the primary and secondary cores in multicore nanoparticle systems are associated with individual particles and clusters, respectively. As shown in Fig. 3, transmission electron microscopy (TEM) images confirm that the individual particle sizes of samples S0 and S1 are comparable to D_p in Table I, while also highlighting a broad particle-size distribution. The TEM images identified large clustered particles in sample S1 and small aggregates in sample S0. However, the high electrostatic repulsion of the anionic surfactant in sample S0 should prevent particle aggregation induced by the magnetic interactions of the large particles [32]. In terms of colloidal properties, Table I shows the small hydrodynamic diameter (D_s) of sample S0 estimated using low-frequency AC susceptometry. The corresponding high ratio of D_p/D_s is a key factor in treating sample S0 as a single-core nanoparticle system, in addition to the single-mode moment distribution (Fig. 2). A $D_p/D_s \approx 1$ corresponds to ideal core-shell structures. In contrast, Fig. 3 shows sample S1 as a model of multicore nanoparticle system with small D_p/D_s. Magnetic fractionation did not significantly change D_p/D_s for samples S2 and S3 (Table I).

C. Broadband AC susceptometry

Similar to FMR spectroscopy [33], the AC magnetic susceptibilities of all solid samples were measured using a vector network analyzer (VNA N5230A, Keysight Technologies, USA) at frequencies ranging from 0.1 to 26.5 GHz at room temperature. The intermediate-frequency bandwidth and averaging factor were set to 500 Hz and 5, respectively. As illustrated in Fig. 4, we used a shielded measurement fixture of a short-circuited microstrip line (MSL) connected to the VNA via subminiature type A (SMA) connector [34,35].
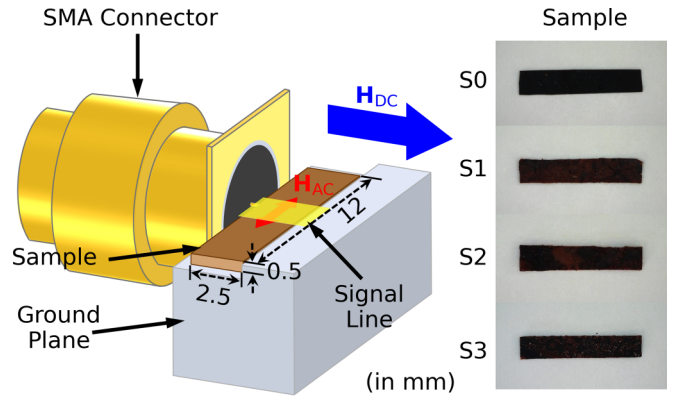

FIG. 4. Measurement fixture of microwave susceptibility with a short-circuited microstrip line (MSL). The dimension and the position of MSL have been optimized to maintain a $50\,\Omega$ impedance, while an upper cover completes the fixture to suppress radiation losses and external noises. The sample was positioned across the signal line; thus, the probing $\mathbf{H}_{\mathrm{AC}}$ field was perpendicular to the polarizing $\mathbf{H}_{\mathrm{DC}}$ field.

The nanoparticle samples were shaped into cuboids with dimensions of $2.5\,\mathrm{mm} \times 12\,\mathrm{mm} \times 0.5\,\mathrm{mm}$ to fit into the MSL jig and obtain a high signal-to-noise ratio. The amplitude of the probing field ($\mathbf{H}_{\mathrm{AC}}$) was approximately $0.7\,\mu\mathrm{T}/\mu_0$, where μ_0 is the permeability of free space. An additional DC magnetic field $\mathbf{H}_{\mathrm{DC}}$ was applied perpendicularly to $\mathbf{H}_{\mathrm{AC}}$ (in parallel with the signal line of the MSL) while varying its intensity at $\mu_0 H_{\mathrm{DC}} = 13, 27, 48, 120, 200,$ and $300\,\mathrm{mT}$. Permanent magnets with diameters of $20\,\mathrm{mm}$ were used to adjust H_{DC}, resulting in slight field inhomogeneity depending on the distance between the sample and the magnets. The standard error of H_{DC} along the $12\,\mathrm{mm}$ lateral direction of the sample was below $5\,\%$. Nevertheless, $\mathbf{H}_{\mathrm{DC}}$ should be uniform within the effective region of homogeneous $\mathbf{H}_{\mathrm{AC}}$ at a radius of $2.5\,\mathrm{mm}$ relative to the MSL.

IV. RESULTS

A. DC field-dependent microwave susceptibility spectra

The DC fields applied to a typical single-core magnetic nanoparticle system (i.e., sample S0) appear to change the frequency-dependent complex susceptibility in the microwave range, demonstrating two basic properties: the FMR frequency shift and the symmetric dispersion of $\chi''(\chi')$, as shown in Fig. 5 (first-column panels). Anisotropy and dipolar interactions contribute to the internal field ($\mathbf{H}_{\mathrm{int}}$), which triggers intrinsic FMR in the presence of thermal disturbances. At $H_{\mathrm{DC}} = 0$ and $\mathbf{H}_{\mathrm{eff}} \approx \mathbf{H}_{\mathrm{int}}$, the real part of susceptibility (χ') in sample S0 drops to 0 at the FMR frequency $f_r = 2.40\,\mathrm{GHz}$, whereas the imaginary part (χ'') maximizes at the Larmor frequency $f_0 = 1.46\,\mathrm{GHz}$. Similarly, intrinsic FMR was also observed in samples S1, S2, and S3 (i.e., multicore nanoparticle systems), with f_r and f_0 values of $(1.78, 1.46), (1.71, 1.46),$ and $(2.30, 1.17)\,\mathrm{GHz}$, respectively. Theoretically, the FMR and Larmor frequencies should be nearly identical to consider a small damping factor for the moment precession. However, size-dependent relaxation also contributes to broadening χ'' at low frequencies, creating an
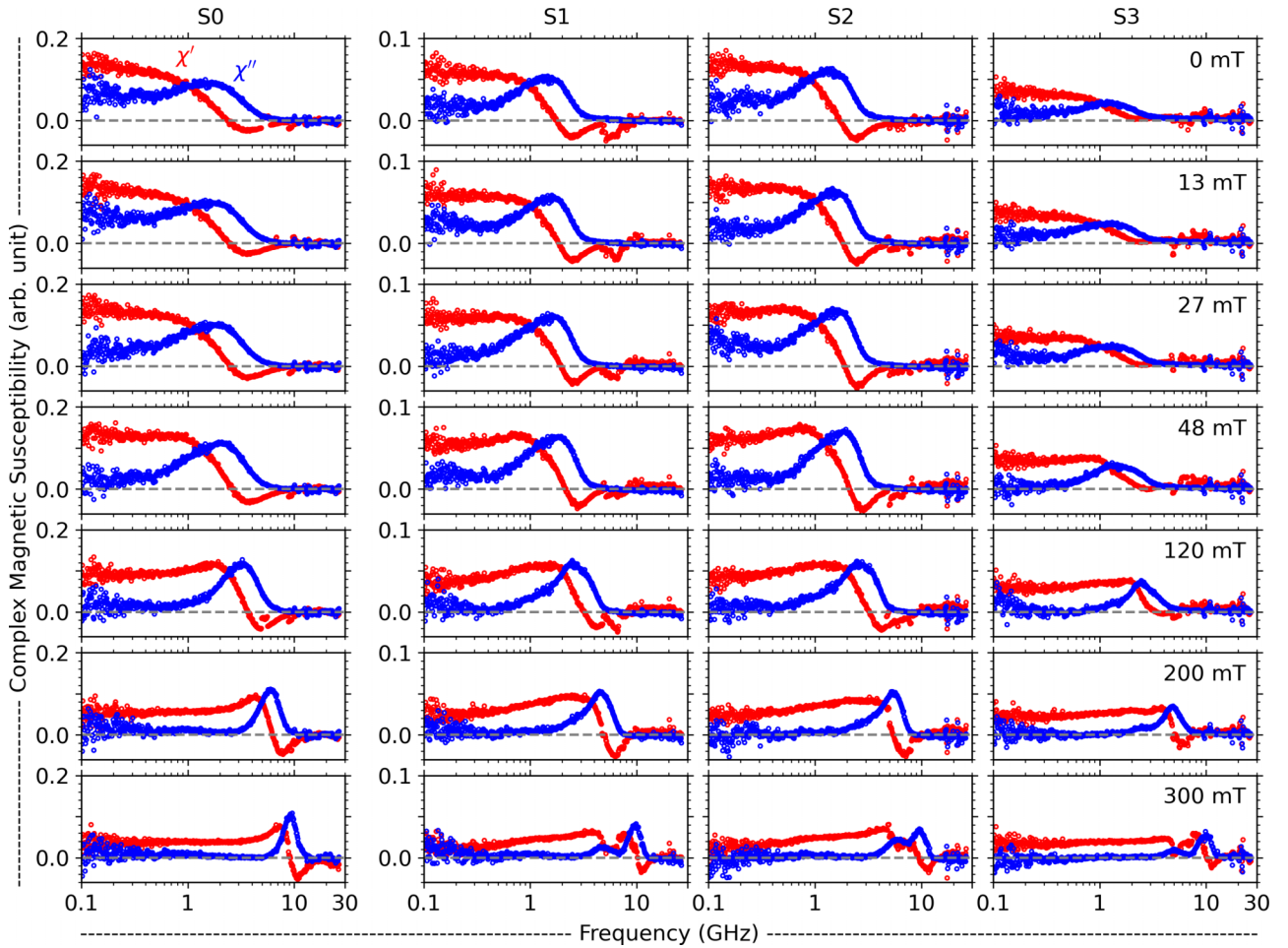
FIG. 5. DC field-dependent complex susceptibility (χ) of the 2.5 mm $\times$ 12 mm $\times$ 0.5 mm solid samples S0, S1, S2, and S3 measured at microwave frequencies ranging from 0.1 to 26.5 GHz. Red and blue circles denote the real (χ') and imaginary (χ'') parts of the susceptibility, respectively. χ was probed under DC fields with varying magnitudes from $H_{\mathrm{DC}} = 0$ (first-row panels) up to $H_{\mathrm{DC}} = 300$ mT$/\mu_0$ (seventh-row panels).

asymmetry in the susceptibility dispersion [36]. From Fig. 5 (first-row panels), we find that $\chi'' > 0$ for $f < 1$ GHz is attributable to moment relaxation.

Figure 5 further highlights that the characteristic f_r and f_0 frequencies demonstrate a blueshift for larger H_{DC}. For $H_{\mathrm{DC}} \leqslant 48$ mT$/\mu_0$, the effects of moment relaxation on increasing χ'' were still observable below 1 GHz. In the case of sample S0, high DC fields with $H_{\mathrm{DC}} \geqslant 200$ mT$/\mu_0$ result in a narrowing peak of χ'' and a more symmetric dispersion of $\chi''(\chi')$. Due to the large energy barrier that suppresses the thermal relaxation of magnetic moments, f_0 is close to f_r at $H_{\mathrm{DC}} = 300$ mT$/\mu_0$, enabling the estimation of α. Meanwhile, the FMR frequency spectra of samples S1 and S2 at higher DC field magnitudes of $H_{\mathrm{DC}} \leqslant 200$ mT$/\mu_0$ are relatively similar. Although these samples exhibit a wide bimodal moment distribution, their primary and secondary cores do not differ significantly. Sample S1 has a lower fraction of large cluster moments than does sample S2 (Fig. 2). This property may be responsible for the different FMR frequency spectra at $H_{\mathrm{DC}} = 300$ mT$/\mu_0$. In the case of sample S3, small cluster moments appear to decrease χ' and χ'' values compared to other multicore nanoparticle samples. From Fig. 2, we can estimate the mean cluster moments of samples S1, S2, and

S3 as $5.75 \times 10^{-19}, 5.31 \times 10^{-19}$, and 2.23×10^{-19} A m^2, respectively.

Unlike sample S0, which consists of single-core nanoparticles, we observed two neighboring χ'' peaks in samples S1, S2, and S3 at $H_{\mathrm{DC}} = 300$ mT$/\mu_0$. As shown in Fig. 5 (seventh-row panels), the first and second χ'' peaks for these three samples were (10.18, 4.90), (9.40, 5.99), and (10.08, 5.00) GHz, respectively. Despite different values of f_0, the first χ'' peak can be attributed to the intrinsic properties of iron-oxide cores. Sample S0 has a single χ'' peak at $f_0 = 9.21$ GHz, which is relatively close to those of the other samples. Particle clustering further suggests that the second χ'' peak at a lower frequency corresponds to the resonance behavior of multicore structures at different effective fields due to magnetic interactions [27]. The demagnetization field distribution in the monodomain state of a cluster potentially leads to inhomogeneous effective fields, which are responsible for multimode FMR spectra [37].

B. Characteristics of FMR requency pectra

Figure 5(a) shows that the large core size of sample S0 leads to a higher magnetization response than the

other samples in terms of the absolute susceptibility, $\chi = (\chi'^2 + \chi''^2)^{1/2}$. For $\mathbf{H}_{DC} \perp \mathbf{H}_{AC}$ and $H_{DC} \gg H_{AC}$, the resultant torque aligns the magnetic moments toward $\mathbf{H}_{DC}$. Thus, the magnetization component parallel to $\mathbf{H}_{AC}$ decreases proportionally, particularly at $f < 1$ GHz, where nonresonant moment relaxation occurs. As the energy barrier increases under higher DC fields (e.g., above $120\,\text{mT}/\mu_0$), the polarized moments begin to precess around the effective field when the AC field frequency matches the Larmor frequency (f_0). This further increases the apparent magnetization response due to the resonance mechanism [38].

When a static field is applied along the z axis and a microwave field along the x axis simultaneously [Fig. 1(b)], spherical cores with the same axial demagnetizing factors ($N_x = N_y = N_z = \frac{1}{3}$) have f_0 linearly dependent on the external static field, $\mathbf{H}_z = \mathbf{H}_{DC} + \mathbf{H}_a$ [15]. Particle faceting and elongation may further affect the anisotropy field ($\mathbf{H}_a$) because the effective demagnetizing factor $N_{eff} = N_x - N_z = N_y - N_z$ is nontrivial [39]. The magnitude of the anisotropy field is often defined as $H_a = 2K_u/(\mu_0 M_s)$ for particles with identical sizes and uniform orientations of the anisotropy axes, whereas the effective field due to dipolar interactions (i.e., the demagnetization field H_d) is simplified to $N_{eff} M_s$ [20]. Therefore, for regular ellipsoidal cores with $N_{eff} \neq 0$, the Larmor frequency is governed by

$$f_0 = \frac{\gamma \mu_0}{2\pi}\Big(H_{DC} + \frac{2K_u}{\mu_0 M_s} + N_{eff} M_s\Big), \qquad (5)$$

where $\gamma/(2\pi)$ is equal to $28.02\,\text{GHz}\,\text{T}^{-1}$.

To investigate whether magnetic interactions contributed to the FMR frequency spectra, we used Eq. (5), assuming spherical cores with $N_{eff} = 0$ for samples S0 and S1. The corresponding M_s values are 410.1 and 324.3 kA m^{-1} (Table I), while approximate values of the anisotropy constant (K_u) for Fe_3O_4 and γFe_2O_3 cores are 16.1 and 8.2 kJ m^{-3}, respectively [40,41]. Sample S1 contains noncrystallized particle clusters, so the K_u of the cores is apparently larger than that of the clusters [41]. We then obtained $H_a = 78.5$ and $50.4\,\text{mT}/\mu_0$, predicting the intrinsic FMR at $f_0 = 2.20$ and 1.41 GHz for samples S0 and S1, respectively. From Fig. 6(b), the measured f_0 appears to be inconsistent with the values calculated using Eq. (5) for $N_{eff} = 0$. This estimate is relatively close to the f_r value. The local fields within clusters that affect $\mathbf{H}_{eff}$ deviate f_0 from the theoretical resonance model [27]. This result validated the significant contribution of magnetic interactions to the field-dependent FMR characteristics.

Figure 6(c) points out that the $f_0/f_r \ll 1$ ratio at low DC fields is a consequence of thermal relaxation, where the magnetic moments of primary cores rotate incoherently inside their clusters. As the DC field increased, the thermal relaxation of the polarized moments became insignificant. Meanwhile, Fig. 6(c) also shows large values of $\Delta f_{FWHM}/f_0$ at $H_{DC} \leqslant 48\,\text{mT}/\mu_0$, indicating a broadening $\chi''(f)$. Here, Δf_{FWHM} is evaluated from the full width at half-maximum of the measured χ'' peak as a function of frequency. The intrinsic FMR (at $H_{DC} = 0$) of sample S0 demonstrates a larger f_{FWHM}/f_0 than that of the other samples, attributed to large K_u [41]. Under $H_{DC} \geqslant 120\,\text{mT}/\mu_0$, $\Delta f_{FWHM}/f_0$ further decreases for all samples as the FMR dominates over the moment relaxation.
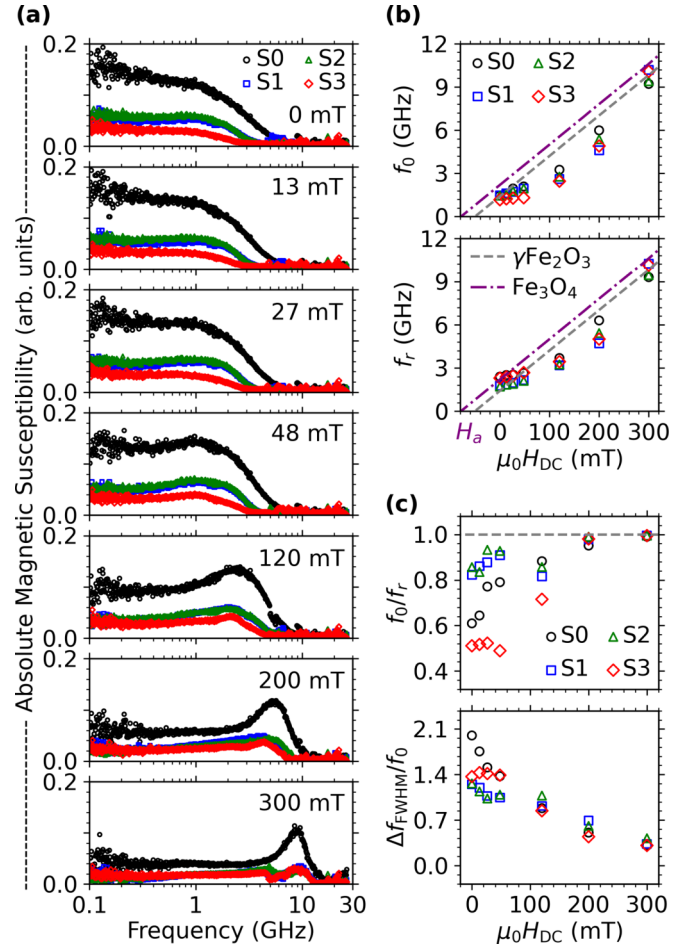

FIG. 6. (a) Microwave moment dynamics in terms of frequency-dependent absolute susceptibility $\chi = (\chi'^2 + \chi''^2)^{1/2}$, under various DC magnetic fields. Open circles, squares, triangles, and diamonds represent samples S0, S1, S2, and S3, respectively. (b) Field-dependent Larmor frequency (f_0) maximizing χ'' (top panel) and FMR frequency (f_r) inverting sign of χ' (bottom panel) at GHz range. Dashed-dotted and dashed lines are values of Eq. (5) for spherical magnetite and maghemite nanoparticles computed with K_u equals 16.1 and 8.2 kJ m^{-3}, respectively. (c) Field-dependent f_0/f_r and $\Delta f_{FWHM}/f_0$ ratios. Δf_{FWHM} is the full width at half-maximum of the measured χ'' peak.

moment relaxation. Consequently, $H_{DC} \gg H_a + H_d$ results in $f_0/f_r \approx 1$, considering only moment precession with a finite damping constant.

C. Relaxation time constant of core particles

The Gilbert damping factor α of the samples can be estimated from the empirical relationship between f_0 and f_r measured in a large DC field, as shown in Eq. (6) [42]:

$$\alpha = \left[\frac{1 - (f_0/f_r)^2}{1 + (f_0/f_r)^2}\right]^{\frac{1}{2}}. \qquad (6)$$

From Fig. 6(c), we obtained $\alpha = 0.10$ at $300\,\text{mT}/\mu_0$ for sample S0, which is comparable to the reported value for magnetite nanoparticles [16]. The other (maghemite) samples have an identical $\alpha = 0.07$. The characteristic time constant

TABLE II. Magnetic properties of core particles related to Néel relaxation.

Sample	α	τ_0 (ns)	σ	τ_N (ns)	f_N (MHz)
S0	0.10	0.72	3.36	10.10	15.8
S1	0.07	1.59	0.30	0.53	298.7
S2	0.07	1.54	0.31	0.54	295.2
S3	0.07	1.73	0.19	0.36	445.9

for thermal relaxation can then be approximated as $\tau_0 = M_s/(2\alpha\gamma K_u)$, thereby obtaining τ_N according to Eq. (3). As shown in Table II, $f_N = (2\pi\tau_N)^{-1}$ for sample S0 should be far below the measurement range of the microwave susceptibility due to the large anisotropy energy, whereas samples S1, S2, and S3 may have moment relaxation overlapping with the intrinsic FMR.

For multicore nanoparticles, thermal relaxation in a field-free environment mainly derives τ_N from the intrinsic dipolar magnetism, where the magnetic moment of each primary core interacts as a single macrospin equivalent to the cluster moment within an activation diameter [29,30]. The resulting effective core size is sufficiently large to exhibit a linear decrease of $\chi'_\parallel$ as a function of $\ln(f)$ (Appendix A). However, fast relaxation of primary cores should increase imaginary susceptibility at microwave frequencies because the core size is expected to be a few nanometers [8,30,41].

The calculated relaxation frequencies of samples S1, S2, and S3 are above 0.29 GHz (Table II). However, Fig. 5 shows no χ'' peak for $f < 1$ GHz in the microwave susceptibility measurement at zero DC field. Thermal disturbance increases the effective damping of the moment dynamics and later causes a decrease in the amplitude of the gyroscopic motion [43,44]. This situation can be avoided by applying a large DC field such that the moment precession dominantly contributes to the apparent magnetization response. An external DC field reduces the absolute susceptibility attributed to Néel relaxation with a shorter time constant [40]. For instance, at $H_{\text{DC}} = 300$ mT/μ_0, χ at 1 GHz decreases by more than half its original value in the absence of a DC field. Moreover, for $f = f_r \gg f_N$, thermal relaxation is negligible, allowing moment precession to maximize χ [Fig. 6(a)].

V. DISCUSSION

In terms of the complex magnetic susceptibility, we hypothesized that the microwave magnetization response of a multicore nanoparticle system collectively takes either moment relaxation or precession to describe the intrinsic FMR in the absence of external DC fields (Fig. 5). Upon applying a sufficiently high DC field, two neighboring χ'' peaks in the susceptibility spectra indicate that anisotropy and dipolar interactions remain significant, yielding inhomogeneous local fields within the multicore superstructures. This observation is similar to the multimode resonance associated with different demagnetization field distributions at the center and edges of the structures [37,45,46]. As an alternative to micromagnetic modeling, we discuss the microwave susceptibility spectra with the distribution functions of magnetic nanoparticles.

A. Distributive damping factors, resonance frequencies, and internal fields

To fit the measurement results shown in Fig. 5, we empirically generalized frequency-dependent microwave susceptibility into $\chi(\omega) = c_\parallel\chi_\parallel(\omega) + c_\perp\chi_\perp(\omega)$, where $c_\parallel$ and $c_\perp$ are arbitrary constants related to the significance of relaxation and precession in defining moment dynamics. Theoretically, $c_\parallel$ and $c_\perp$ are $\frac{1}{3}$ and $\frac{2}{3}$, respectively, for monodisperse particles [47]. However, the size and moment distributions of the particles vary with the relaxation time, damping factor, and internal fields. Therefore, we adopted Eq. (2) to define the real and imaginary parts of the parallel susceptibility attributed to the Néel relaxation as follows:

$$\chi'_\parallel(\omega) = \sum_{j=1}^{2}\sum_{i=1}^{N}\frac{a_j\rho_{m,ij}m_{p,i}}{1+(\omega\tau_{N,ij})^2} + a_0 \qquad (7)$$

and

$$\chi''_\parallel(\omega) = \sum_{j=1}^{2}\sum_{i=1}^{N}\frac{a_j\rho_{m,ij}m_{p,i}\omega\tau_{N,ij}}{1+(\omega\tau_{N,ij})^2}, \qquad (8)$$

respectively. a_0 in Eq. (7) is an arbitrary constant that limits the high-frequency susceptibility, whereas a_j represents the fraction of moment relaxation in the primary and secondary cores. Equations (7) and (8) explore $\tau_{N,ij}(\sigma_{ij}, H_{\text{DC}})$ for each moment $m_{p,i}$. In this case, $\tau_{N,ij}(\sigma_{ij}, 0)$ satisfies the low-frequency susceptibility spectra obtained by substituting the anisotropy-to-thermal energy ratio σ_i into Eq. (3) (see Appendix A). We used the empirical relationship $(1 + 1.97\xi^{3.18})^{-0.5}$ to approximate $\tau_{N,ij}(\sigma_{ij}, H_{\text{DC}})/\tau_{N,ij}(\sigma_{ij}, 0)$ for ξ denoting static magnetopotential as $\bar{m}_p H_{\text{DC}}/(k_B T)$ [40].

To describe the change in the FMR frequency spectra for $H_{\text{DC}} \perp H_{\text{AC}}$, the real and imaginary components of perpendicular susceptibility are governed by Eq. (4) as follows:

$$\chi'_\perp(\omega) = \gamma\sum_{j=1}^{2}\sum_{i=1}^{N}\frac{b_j\rho_{m,ij}m_{p,i}\left[\omega_{0,ij}^2 - \omega^2\left(1-\alpha_i^2\right)\right]}{\left[\omega_{0,ij}^2 - \omega^2\left(1+\alpha_i^2\right)\right]^2 + 4\alpha_i^2\omega_{0,ij}^2\omega^2}$$

$$(9)$$

and

$$\chi''_\perp(\omega) = \gamma\sum_{j=1}^{2}\sum_{i=1}^{N}\frac{b_j\alpha_i\rho_{m,ij}m_{p,i}\left[\omega_{0,ij}^2 + \omega^2\left(1+\alpha_i^2\right)\right]}{\left[\omega_{0,ij}^2 - \omega^2\left(1+\alpha_i^2\right)\right]^2 + 4\alpha_i^2\omega_{0,ij}^2\omega^2},$$

$$(10)$$

respectively. The damping factor α_i is specific to each value of $m_{p,i}$. Here, Eqs. (9) and (10) show that $\omega_{0,ij} = \gamma(H_{\text{DC}} + H_{\text{int},ij})$ depends on the core and cluster moments with different $\rho_{m,ij}$ values for each jth subdistribution of multicore nanoparticles (Fig. 2). The magnitude of the internal field (H_{int}) also changes with increasing DC field. The dual $\chi'' \approx \chi''_\perp$ peaks at neighboring frequencies are approached by Eq. (10), where the resonance intensities attributed to ω_0 distributions of the individual cores and clusters are weighted by b_j proportionally.

Figure 7(a) demonstrates the curve fitting of $\chi(\omega)$ for $H_{\text{DC}} = 0$ and 300 mT/μ_0. This further proves that $\chi_\parallel(\omega)$ due to Néel relaxation can significantly increase $\chi(\omega)$ at $f < 1$ GHz in the absence of an external DC field, whereas
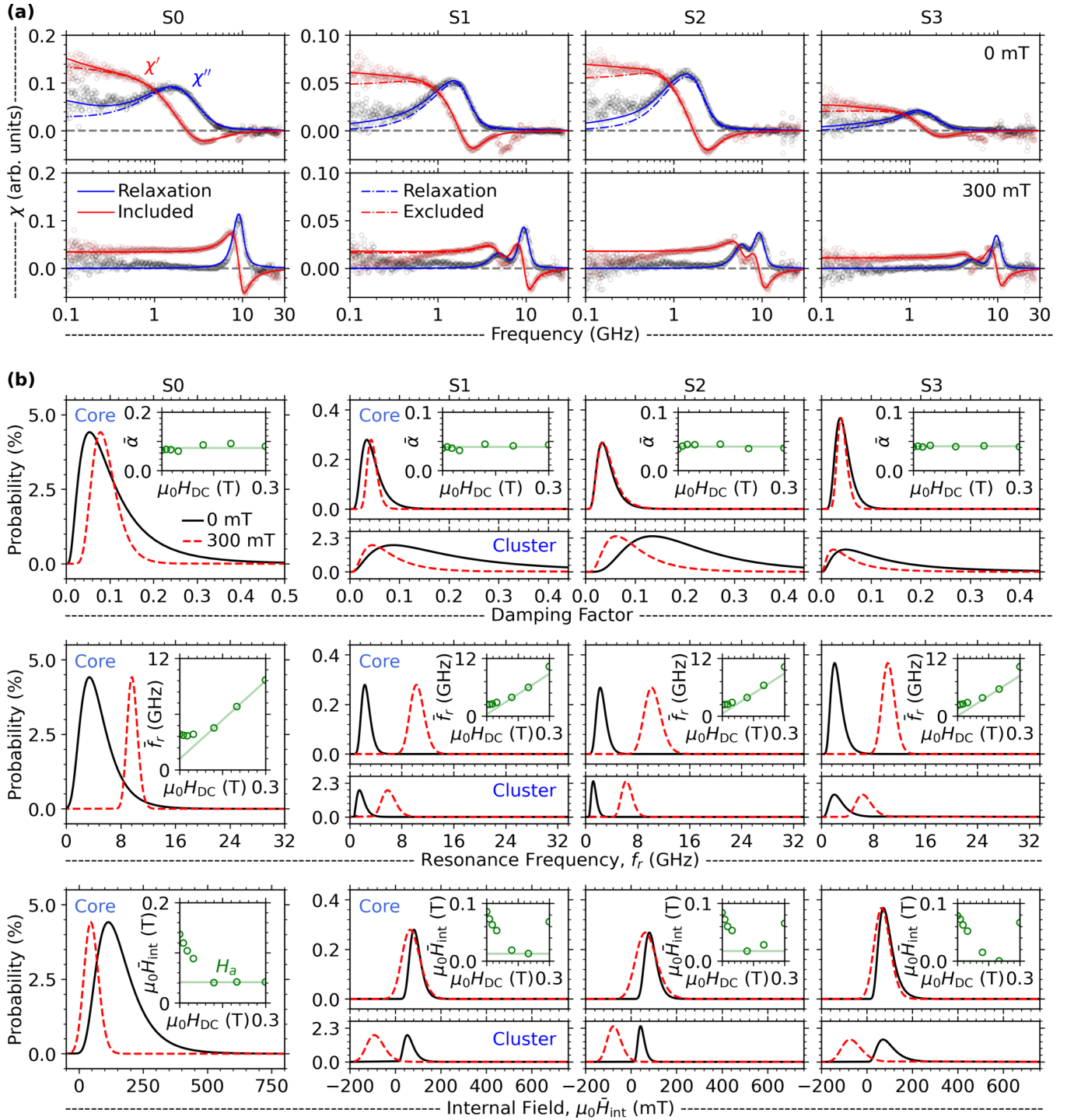
FIG. 7. (a) Curve fitting of FMR frequency spectra at $\mu_0 H_{DC} = 0$ and 300 mT using Eqs. (7)–(10). Solid lines represent the χ' and χ'' values calculated by including thermal relaxation to fit the measurement data (open circles). Dashed-dotted lines are the values computed using the LLG-Kittel model only. (b) Distribution functions of damping factor, resonance frequency, and internal field to estimate susceptibility spectra under $H_{DC} = 0$ (solid lines) and 300 mT/μ_0 (dashed lines). Inset figures of $\bar{\alpha}$, $\bar{f}_r$, and $\bar{H}_{int}$ are the mean values of distributive damping factors, resonance frequencies, and internal fields, respectively.

a high H_{DC} results in $\chi(\omega) \approx \chi_\perp(\omega)$. At $f < 0.5$ GHz, the fluctuating $\chi(\omega)$ values are attributable to measurement noise. From numerical analysis using Eqs. (9) and (10), we obtain the log-normal distributions of α, f_r, and H_{int} for each H_{DC} as shown in Fig. 7(b). For example, in sample S0, α initially varies from 0.0 to 0.5 at $H_{DC} = 0$ and has a narrower

distribution at 300 mT/μ_0 [first-column panels of Fig. 7(b)]. However, the mean value of the damping factors ($\bar{\alpha}$) was relatively constant at 0.078, which was more accurate than the value obtained from the graphical analysis of the measurement data (Table II). Meanwhile, $f_r = f_0(1 - \alpha^2)^{-0.5} \approx f_0$ is distributed within the measured FMR bandwidth. Because
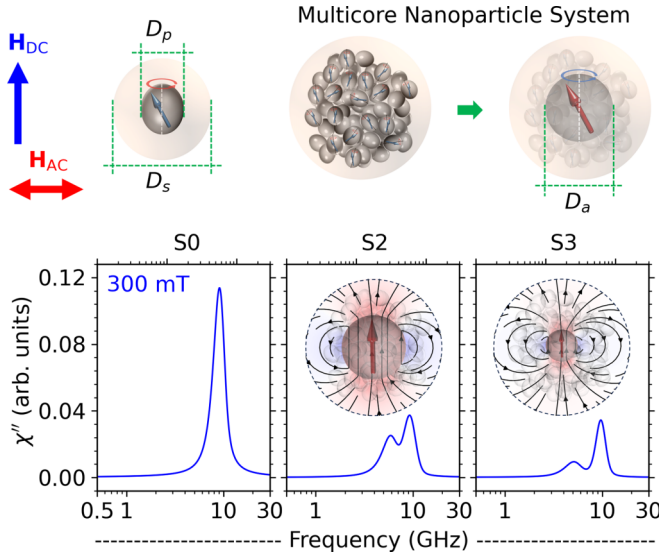
FIG. 8. Dual-mode FMR frequency spectra of multicore nanoparticle system due to an inhomogeneous distribution of local demagnetization field under $H_{DC} = 300\,\text{mT}/\mu_0$. D_a is an activation diameter where the primary core particles behave collectively as a single macrospin with large magnetic moment.

we plotted the mean resonance frequency ($\bar{f}_r$) as a function of H_{DC}, we can estimate H_a to be $41.23\,\text{mT}/\mu_0$ for sample S0. In terms of the H_{int} distribution, H_a can be treated as the minimum value of the field-dependent mean internal field $\bar{H}_{int}(H_{DC})$.

For samples S1, S2, and S3, a bimodal distribution of magnetic moments was adopted to fit the FMR frequency spectra using Eqs. (9) and (10). This curve fitting provided the different properties of α, f_r, and H_{int} distributions for the cores and clusters [Fig. 7(b)]. For the three samples, $\bar{\alpha}$ of the core particles is independent of H_{DC} with a constant value of 0.041. The corresponding f_r distribution at $300\,\text{mT}/\mu_0$ appears broader than that of sample S0 because the cluster structures affect the H_{int} distribution in terms of the demagnetization fields. The third-row panels in Fig. 7(b) show that the distributed H_{int} of the clusters is negative at $300\,\text{mT}/\mu_0$, where $\mathbf{H}_{int}$ opposes the direction of $\mathbf{H}_{DC}$. The local reduction in the effective field inside the cluster structures further correlates with a lower f_r. Therefore, unlike sample S0 with a single χ'' peak, samples S1, S2, and S3 demonstrate dual-mode FMR frequency spectra at high DC field.

B. Dual-mode FMR frequency spectra of multicore nanoparticles

The inhomogeneous demagnetization field distribution under high DC field can create local regions with different effective field magnitudes (H_{eff}), resulting in multimode FMR frequency spectra with $f_r \propto H_{eff}$. Similarly, we observed two neighboring f_r values for multicore nanoparticles, in which secondary f_r appeared to be dependent on the cluster moments (m_c), as shown by samples S2 and S3 (Fig. 8). To support our findings, we assume a spherical activation volume for the secondary cores with a diameter of $D_a = [6m_c/(\pi M_s)]^{1/3}$, where the magnetic moments of the primary core particles

are collaterally aligned in the direction of $\mathbf{H}_{DC}$ and behave collectively as a single macrospin. Here, D_a is approximately 14.76 and 10.64 nm for samples S2 and S3, respectively. For $D_p < D_a < D_s$, Fig. 8 illustrates that $m_c > m_p$ yields demagnetization fields outside the area of D_a, which can potentially reduce H_{eff} in a finite area within D_s. For relatively similar D_s, the large m_c of sample S2 proportionally creates a demagnetized area and splits the FMR frequency spectra, with larger χ'' of the secondary mode than that of sample S3.

Multicore magnetic nanoparticles obtained by hydrodynamic particle clustering are typically nonspherical and have complex structures, complicating their field-dependent magnetization dynamics (Fig. 3). Our work shows a physical phenomenon in which a high DC field induces dual-mode FMR frequency spectra in multicore nanoparticle systems, emphasizing discretized areas inside clusters with distinctive H_{eff} due to an inhomogeneous demagnetization field distribution. Although micromagnetic modeling of multicore nanoparticle systems is necessary to further validate this hypothesis, a simple field simulation of a spherical nanoparticle highlighted opposite demagnetization fields near the particle (Fig. 8). In addition to computational studies, more detailed FMR experiments may provide valuable insights into the ultrafast moment dynamics in multicore nanoparticle system for biomedical applications.

VI. CONCLUSION

We measured the DC field-dependent microwave susceptibility to characterize the fast moment dynamics of single-core and multicore magnetic nanoparticle systems in correlation with the FMR frequency spectra. Four samples with an iron concentration of $46\,\text{mg}_{Fe}\,\text{mL}^{-1}$ were solidified with epoxy resin and shaped into cuboids of $2.5\,\text{mm} \times 12\,\text{mm} \times 0.5\,\text{mm}$. This configuration allowed Néel relaxation to initially define the low-frequency magnetization response. Above 0.1 GHz, we observed that FMR mainly contributed to the apparent complex susceptibility spectra, although thermal relaxation was not trivial below 1 GHz. While both phenomena resulted in a collective magnetization response, the introduction of external DC fields led to a unique FMR shift. Single-core nanoparticle system exhibited a unitary FMR frequency that shifted to higher frequencies with increasing DC fields, whereas multicore nanoparticle system showed a secondary peak of imaginary susceptibility close to the intrinsic FMR frequency, particularly at 300 mT.

We numerically fitted the dual-mode FMR frequency spectra of multicore nanoparticles using the LLG-Kittel equation, considering the moment distribution and its correlation with the damping factor and the Larmor frequency. We modeled a computation in which the first satellite FMR peak was attributed to secondary cores with a broad distribution of gyroscopic parameters, whereas the latter peak corresponded to the moment precession of the primary cores. The results affirm a possible mechanism by which nonuniform effective fields experienced by multicore magnetic nanoparticles lead to local synchronous moment precession below the Larmor frequency of a typical spin gyration in an individual core. Understanding these characteristics encourages an in-depth investigation of how the morphology of such nanostructures
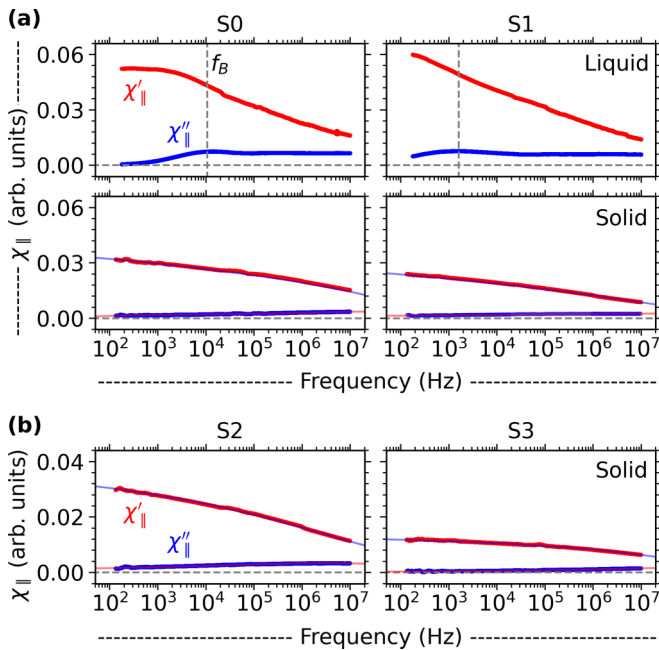
FIG. 9. Low-frequency complex (parallel) susceptibility of all samples with $46\,\mathrm{mg_{Fe}\,mL^{-1}}$ iron concentration. The real ($\chi'_\parallel$) and imaginary ($\chi''_\parallel$) parts are depicted in red and blue colors. (a) $\chi'_\parallel$ and $\chi''_\parallel$ of liquid (first row) and solid (second row) samples for S0 and S1. Vertical dashed line indicates the Brownian relaxation frequency (f_B). (b) $\chi'_\parallel$ and $\chi''_\parallel$ of solid samples for S2 and S3. No observable $\chi''_\parallel$ peak indicates the Néel relaxation should be above 10 MHz. Transparent solid lines represent the values calculated using Eqs. (7) and (8).

contributes to high-frequency magnetic losses, particularly in microwave-assisted hyperthermia applications.

APPENDIX A: LOW-FREQUENCY COMPLEX MAGNETIC SUSCEPTIBILITY

In order to characterize the relaxation behavior of the samples, an extended low-frequency susceptibility ($\chi_\parallel$) was measured by a frequency response analyzer (FRA51615, NF Corporation, Japan) ranging from 100 Hz to 10 MHz. We applied an AC magnetic field ($\mathbf{H}_{AC}$) with magnitude $\mu_0 H_{AC} = 0.1\,\mathrm{mT}$ to the liquid and solid samples, in which a pickup coil was aligned concentrically to the excitation coil [48]. As shown in the first-row panels of Fig. 9(a), we identified $\chi''_\parallel$ for both liquid samples S0 and S1 maximized at the Brownian relaxation frequency $f_B = 10.7$ and 1.6 kHz, respectively. The corresponding hydrodynamic diameters (D_s) are equal to 30.5 and 58.5 nm, while considering the medium viscosity of 1.35 and 1.28 mPa s at $T = 295\,\mathrm{K}$. Samples S2 and S3 were supposed to have a similar D_s with sample S1 [30].

The magnetization in the liquid samples significantly decreases at high frequencies since large friction forces inhibit Brownian rotation, resulting in an incomplete easy-axis
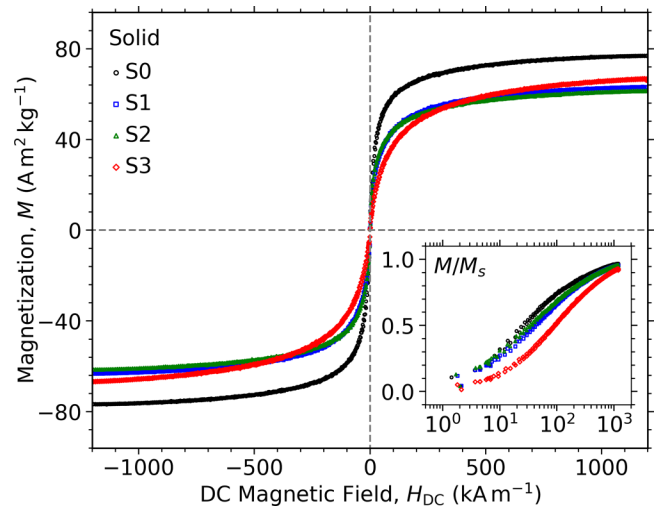

FIG. 10. DC field-dependent specific magnetization properties of $2.5\,\mathrm{mm} \times 12\,\mathrm{mm} \times 0.5\,\mathrm{mm}$ solid samples with $46\,\mathrm{mg_{Fe}\,mL^{-1}}$ iron concentration measured by VSM at room temperature. No coercivity was observed in all samples. The inset further emphasizes the nonlinearity of M/M_s, which is a normalized magnetization relative to each saturation value.

relaxation [11]. This situation reduces the disparity in magnetization response between the solid and liquid samples, where the Néel relaxation becomes dominant. For solid samples S0 and S1 with randomly oriented easy axes, $\chi'_\parallel$ decreases linearly with increasing $\ln(f)$, while $\chi''_\parallel$ shows no peak across the measurement frequency [second-row panels of Fig. 9(a)]. We obtained similar results for the case of solid samples S2 and S3. Figure 9(b) further highlights a significant susceptibility difference between these samples, which is attributable to the proportion of secondary cores (with large moments) in each sample.

APPENDIX B: STATIC MAGNETIZATION RESPONSE

The total mass (including epoxy resin) for samples S0, S1, S2, and S3 was 15.5, 14.0, 15.6, and 14.4 mg. respectively, whereas the iron content was prepared at 0.69 mg. Despite having different values of saturation magnetization M_s, all samples exhibited superparamagnetism at room temperature as shown in Fig. 10. For this case, the magnetization M nonlinearly increases at higher H_{DC} static fields, accounting for the sum of each composing magnetic moment m_p over sample volume ν [49]. Based on the nonlinearity of M/M_s, the inset in Fig. 10 further indicates the smaller core sizes of samples S1, S2, and S3 as compared to sample S0. Here, monodomain nanoparticles with large core sizes may easily align their magnetic moments at low external DC field as they have large anisotropy energy. For instance, M/M_s of sample S0 reaches 0.75 at $100\,\mathrm{kA\,m^{-1}}$, whereas the other samples show $M/M_s < 0.66$ for the same H_{DC}. Therefore, the nonlinear field dependence of M/M_s becomes a fundamental feature for assessing size polydispersity in a magnetic nanoparticle system.

In general, multicore magnetic nanoparticles demonstrate a bimodal moment distribution to account for the individual

moments and their resultant for the clustered particles, which have been identified using inverse methods of the field-dependent magnetization curve [29]. As a straightforward analysis, we applied a double-weighted Langevin function ($\mathcal{L}$):

$$\mathcal{L}(m_p, H_{\mathrm{DC}}) = \coth\left(\frac{\mu_0 m_p H_{\mathrm{DC}}}{k_B T}\right) - \frac{k_B T}{\mu_0 m_p H_{\mathrm{DC}}}, \qquad \text{(B1)}$$

to fit $M(H_{\mathrm{DC}})$ as shown in Eq. (B2):

$$M(H_{\mathrm{DC}}) = \frac{1}{2\nu} \sum_{j=1}^{2} \left[\int \rho_{m,j} m_p \mathcal{L}(m_p, H_{\mathrm{DC}}) dm_p \right]. \qquad \text{(B2)}$$

Here, $\rho_{m,1}$ and $\rho_{m,2}$ are the probability density functions of magnetic moments attributed to the primary and secondary cores, respectively with a proportional 1:1 ratio. Equation (B3) notes the log-normal distribution of magnetic moment m_p as follows:

$$\rho_m(m_p) = \frac{1}{\sqrt{2\pi} s_m m_p} \exp\left[- \frac{\ln^2(m_p/m_m)}{2 s_m^2} \right], \qquad \text{(B3)}$$

where s_m is the standard deviation of $\ln(m_p)$, m_m and $m_m \exp(s_m^2/2)$ are the median and the mean values of m_p, respectively [50,51]. We computed Eqs. (B1) to (B3) with least-squares method to obtain $\rho_m (m_p)$ for each sample and summarized the results in Fig. 2.

---

[1] R. H. Kodama, Magnetic nanoparticles, J. Magn. Magn. Mater. **200**, 359 (1999).

[2] C. P. Bean and J. D. Livingston, Superparamagnetism, J. Appl. Phys. **30**, S120 (1959).

[3] A. G. Roca, L. Gutiérrez, H. Gavilán, M. E. Fortes Brollo, S. Veintemillas-Verdaguer, and M. del Puerto Morales, Design strategies for shape-controlled magnetic iron oxide nanoparticles, Adv. Drug Deliver. Rev. **138**, 68 (2019).

[4] C. Blanco-Andujar, D. Ortega, P. Southern, Q. A. Pankhurst, and N. T. K. Thanh, High performance multi-core iron oxide nanoparticles for magnetic hyperthermia: microwave synthesis, and the role of core-to-core interactions, Nanoscale **7**, 1768 (2015).

[5] J.-H. Lee, B. Kim, Y. Kim, and S.-K. Kim, Ultra-high rate of temperature increment from superparamagnetic nanoparticles for highly efficient hyperthermia, Sci. Rep. **11**, 4969 (2021).

[6] M. Vassallo, D. Martella, G. Barrera, F. Celegato, M. Coïsson, R. Ferrero, E. S. Olivetti, A. Troia, H. Sözeri, C. Parmeggiani, D. S. Wiersma, P. Tiberto, and A. Manzin, Improvement of hyperthermia properties of iron oxide nanoparticles by surface coating, ACS Omega **8**, 2143 (2023).

[7] L. Gutiérrez, L. de la Cueva, M. Moros, E. Mazarío, S. de Bernardo, J. M. de la Fuente, M. P. Morales, and G. Salas, Aggregation effects on the magnetic properties of iron oxide colloids, Nanotechnology **30**, 112001 (2019).

[8] D. Eberbeck, C. L. Dennis, N. F. Huls, K. L. Krycka, C. Gruttner, and F. Westphal, Multicore magnetic nanoparticles for magnetic particle imaging, IEEE Trans. Magn. **49**, 269 (2013).

[9] H. Kratz, M. Taupitz, A. Ariza de Schellenberger, O. Kosch, D. Eberbeck, S. Wagner, L. Trahms, B. Hamm, and J. Schnorr, Novel magnetic multicore nanoparticles designed for MPI and other biomedical applications: From synthesis to first in vivo studies, PLoS One **13**, e0190214 (2018).

[10] A. O. Ivanov and F. Ludwig, Static magnetic response of multi-core particles, Phys. Rev. E **102**, 032603 (2020).

[11] S. Ota and Y. Takemura, Evaluation of easy-axis dynamics in a magnetic fluid by measurement and analysis of the magnetization curve in an alternating magnetic field, Appl. Phys. Express **10**, 085001 (2017).

[12] S. B. Trisnanto, S. Ota, and Y. Takemura, Two-step relaxation process of colloidal magnetic nanoclusters under pulsed fields, Appl. Phys. Express **11**, 075001 (2018).

[13] T. Q. Bui, A. J. Biacchi, C. L. Dennis, W. L. Tew, A. R. Hight Walker, and S. I. Woods, Advanced characterization of magnetization dynamics in iron oxide magnetic nanoparticle tracers, Appl. Phys. Lett. **120**, 012407 (2022).

[14] T. Gilbert, A phenomenological theory of damping in ferromagnetic materials, IEEE Trans. Magn. **40**, 3443 (2004).

[15] C. Kittel, On the theory of ferromagnetic resonance absorption, Phys. Rev. **73**, 155 (1948).

[16] P. Fannin, C. Marin, I. Malaescu, and N. Stefu, An investigation of the microscopic and macroscopic properties of magnetic fluids, Physica B (Amsterdam) **388**, 87 (2007).

[17] W. T. Coffey and P. C. Fannin, Internal and Brownian mode-coupling effects in the theory of magnetic relaxation and ferromagnetic resonance of ferrofluids, J. Phys.: Condens. Matter **14**, 3677 (2002).

[18] T. Kahmann and F. Ludwig, Magnetic field dependence of the effective magnetic moment of multi-core nanoparticles, J. Appl. Phys. **127**, 233901 (2020).

[19] S. Ota and Y. Takemura, Characterization of Néel and Brownian relaxations isolated from complex dynamics influenced by dipole interactions in magnetic nanoparticles, J. Phys. Chem. C **123**, 28859 (2019).

[20] D. Slay, D. Cao, E. C. Ferré, and M. Charilaou, Ferromagnetic resonance of superparamagnetic nanoparticles: The effect of dipole–dipole interactions, J. Appl. Phys. **130**, 113902 (2021).

[21] W. T. Coffey, P. J. Cregg, and Y. U. P. Kalmykov, On the theory of Debye and Néel relaxation of single domain ferromagnetic particles, in *Advances in Chemical Physics* (Wiley, Hoboken, NJ, 2007), pp. 263–464.

[22] E. C. Stoner and E. P. Wohlfarth, A mechanism of magnetic hysteresis in heterogeneous alloys, Philos. Trans. R. Soc. London A **240**, 599 (1948).

[23] W. F. Brown, Thermal fluctuations of a single-domain particle, Phys. Rev. **130**, 1677 (1963).

[24] P. C. Fannin and S. W. Charles, On the calculation of the Néel relaxation time in uniaxial single-domain ferromagnetic particles, J. Phys. D: Appl. Phys. **27**, 185 (1994).

[25] J. Dubreuil and J. Bobowski, Ferromagnetic resonance in the complex permeability of an Fe_3O_4-based ferrofluid at radio and microwave frequencies, J. Magn. Magn. Mater. **489**, 165387 (2019).

[26] Y. Pu, L. Tonthat, T. Murayama, K. Okita, and S. Yabukami, Method for measuring magnetic susceptibility of magnetic nanoparticles up to millimeter-wave frequency range, AIP Adv. **13**, 025129 (2023).

[27] K. Chalapat, J. V. I. Timonen, M. Huuppola, L. Koponen, C. Johans, R. H. A. Ras, O. Ikkala, M. A. Oksanen, E. Seppälä, and G. S. Paraoanu, Ferromagnetic resonance in ϵ-Co magnetic composites, Nanotechnology **25**, 485707 (2014).

[28] P. Fannin, Use of ferromagnetic resonance measurements in magnetic fluids, J. Mol. Liq. **114**, 79 (2004).

[29] T. Yoshida, N. B. Othman, and K. Enpuku, Characterization of magnetically fractionated magnetic nanoparticles for magnetic particle imaging, J. Appl. Phys. **114**, 173908 (2013).

[30] S. B. Trisnanto and Y. Takemura, Effective Néel relaxation time constant and intrinsic dipolar magnetism in a multicore magnetic nanoparticle system, J. Appl. Phys. **130**, 064302 (2021).

[31] P. Ilg, Equilibrium magnetization and magnetization relaxation of multicore magnetic nanoparticles, Phys. Rev. B **95**, 214427 (2017).

[32] L. Gutiérrez, R. Costo, C. Grüttner, F. Westphal, N. Gehrke, D. Heinke, A. Fornara, Q. A. Pankhurst, C. Johansson, S. Veintemillas-Verdaguer, and M. P. Morales, Synthesis methods to prepare single- and multi-core iron oxide nanoparticles for biomedical applications, Dalton Trans. **44**, 2943 (2015).

[33] Y. Endo, O. Mori, Y. Shimada, S. Yabukami, S. Sato, and R. Utsumi, Study on measurement technique for magnetization dynamics of thin films, Appl. Phys. Lett. **112**, 252403 (2018).

[34] S. Takeda, T. Hotchi, S. Motomura, and H. Suzuki, Permeability measurements of magnetic thin films using shielded short-circuited microstrip lines, J. Magn. Soc. Jpn. **39**, 227 (2015).

[35] S. Takeda and M. Naoe, Size optimization for complex permeability measurement of magnetic thin films using a short-circuited microstrip line up to 30 GHz, J. Magn. Magn. Mater. **449**, 530 (2018).

[36] S. B. Trisnanto and Y. Kitamoto, Field-dependent brownian relaxation dynamics of a superparamagnetic clustered-particle suspension, Phys. Rev. E **90**, 032306 (2014).

[37] K. Miyake, S.-M. Noh, T. Kaneko, H. Imamura, and M. Sahashi, Study on high-frequency 3–D magnetization precession modes of circular magnetic nano-dots using coplanar wave guide vector network analyzer ferromagnetic resonance, IEEE Trans. Magn. **48**, 1782 (2012).

[38] M. Jadav and S. P. Bhatnagar, Particle size controlled magnetic loss in magnetite nanoparticles in RF-microwave region, IEEE Trans. Magn. **56**, 1 (2020).

[39] R. Moreno, S. Poyser, D. Meilak, A. Meo, S. Jenkins, V. K. Lazarov, G. Vallejo-Fernandez, S. Majetich, and R. F. L. Evans, The role of faceting and elongation on the magnetic anisotropy of magnetite Fe_3O_4 nanocrystals, Sci. Rep. **10**, 2722 (2020).

[40] J. Dieckhoff, D. Eberbeck, M. Schilling, and F. Ludwig, Magnetic-field dependence of Brownian and Néel relaxation times, J. Appl. Phys. **119**, 043903 (2016).

[41] K. Enpuku, A. L. Elrefai, T. Yoshida, T. Kahmann, J. Zhong, T. Viereck, and F. Ludwig, Estimation of the effective magnetic anisotropy constant of multi-core based magnetic nanoparticles from the temperature dependence of the coercive field, J. Appl. Phys. **127**, 133903 (2020).

[42] P. Fannin, C. Marin, and C. Couper, Precessional decay time of nanoparticles in magnetic fluids, J. Magn. Magn. Mater. **322**, 1682 (2010).

[43] T. A. Ostler, M. O. A. Ellis, D. Hinzke, and U. Nowak, Temperature-dependent ferromagnetic resonance via the Landau-Lifshitz-Bloch equation: Application to FePt, Phys. Rev. B **90**, 094402 (2014).

[44] J. Urquijo, J. Otálora, and O. Suarez, Ferromagnetic resonance of a magnetic particle using the Landau–Lifshitz–Bloch equation, J. Magn. Magn. Mater. **552**, 169182 (2022).

[45] G. Mohler and A. W. Harter, Micromagnetic investigation of resonance frequencies in ferromagnetic particles, J. Appl. Phys. **97**, 10E313 (2005).

[46] N. Neugebauer, T. Hache, M. T. Elm, D. M. Hofmann, C. Heiliger, H. Schultheiss, and P. J. Klar, Frequency- and magnetic-field-dependent properties of ordered magnetic nanoparticle arrangements, Phys. Rev. B **103**, 094438 (2021).

[47] P. C. Fannin, T. Relihan, and S. W. Charles, Experimental and theoretical profiles of the frequency-dependent complex susceptibility of systems containing nanometer-sized magnetic particles, Phys. Rev. B **55**, 14423 (1997).

[48] S. B. Trisnanto and Y. Kitamoto, Distributive activation volumes of magnetically interacting nanostructures, J. Phys. Chem. C **123**, 23732 (2019).

[49] D. V. Berkov, P. Görnert, N. Buske, C. Gansau, J. Mueller, M. Giersig, W. Neumann, and D. Su, New method for the determination of the particle magnetic moment distribution in a ferrofluid, J. Phys. D: Appl. Phys. **33**, 331 (2000).

[50] M. El-Hilo, Nano-particle magnetism with a dispersion of particle sizes, J. Appl. Phys. **112**, 103915 (2012).

[51] P. Bender, C. Balceris, F. Ludwig, O. Posth, L. K. Bogart, W. Szczerba, A. Castro, L. Nilsson, R. Costo, H. Gavilán, D. González-Alonso, I. de Pedro, L. F. Barquín, and C. Johansson, Distribution functions of magnetic nanoparticles determined by a numerical inversion method, New J. Phys. **19**, 073012 (2017).